Chinese Chemical Letters 35 (2024) 108513

Contents lists available at ScienceDirect

Chinese Chemical Letters

journal homepage: www.elsevier.com/locate/cclet

Recent advances in photothermal effects for hydrogen evolution

Pengcheng Fan, Yuhao He, Junan Pan, Ning Sun, Qiyu Zhang, Chen Gu, Kang Chen, Weinan Yin, Longlu Wang*

College of Electronic and Optical Engineering & College of Flexible Electronics (Future Technology), Nanjing University of Posts & Telecommunications (NUPT), Nanjing 210023, China

ARTICLE INFO

Article history:
Received 21 January 2023
Revised 25 March 2023
Accepted 24 April 2023
Available online 29 April 2023

Keywords:
Photothermal effect
H_2 evolution reaction
Photothermal catalysis
Water vapor splitting
Environmental restoration

ABSTRACT

Photothermal effect has been widely employed in the H_2 evolution process at the advantage of using clean energy sources to produce another one of higher benefits. The solar-to-heat conversion have various forms and heat can facilitate reactions in a variety of dimensions. Hence, summarizing the sources and destinations of heat is important for constructing hydrogen production systems of higher efficiency. This view mainly focuses on the recent state-of-art progress of hydrogen evolution reaction (HER) based on photothermal effect. First, we introduce the main pathways of photothermal conversions applied in H_2 evolution. Then, the functions of the photothermal effect are clearly summarized. Furthermore, we go beyond the catalytic reaction and introduce a method to improve the catalytic system by changing the catalytic bulk phase through thermal means. In the end, we sort out the challenges and outlook to offer some noble insights for this promising area.

1. Introduction

Hydrogen energy is widely considered as a clean substitute for fossil fuel in the future [1–6]. Hydrogen generation through two most abundant natural resources, water and solar energy, offers a promising pathway for carbon neutrality [7–9]. Photocatalysis for hydrogen evolution reaction (HER) has been widely studied since the pioneer work done by Fujishima and Honda in 1972 [10–13]. The mechanism of photocatalysis can be encapsulated as: electron-hole pairs excited by incident light migrate respectively to conduction band and valence band of the catalyst. Driven by diffusion or electric field, the carriers move to the surface and participate in the redox reaction [14–16]. However, for most photocatalytic materials, weak absorption of solar spectrum and low apparent quantum efficiency are two main obstacles preventing them from industrial application [17–20].

Recently, more and more researchers put an emphasis on the facilitation effect of thermal engagement and come up with the new conception of photothermal catalysis based on photocatalysis has become a fast-growing research area [21–26]. Literally, photothermal catalysis refers to catalytic reactions involving heat and photo participation [27,28]. In the reported photothermal H_2 evolution process, two main mechanisms of photothermal effect are widely employed: local surface plasmon resonance [29] and thermal conversion of near-infrared absorption of photothermal materials [30].

Photothermal catalysis enjoys great popularity in that about half of the solar spectrum (NIR) can provide heat for catalytic system through thermal radiation while the photocatalytic reaction of semiconductors only utilizes the incident light of higher energy. Moreover, photothermal catalysis can combine the advantages of thermocatalysis and photocatalysis, thereby rendering excellent catalytic performance even under moderate conditions.

As shown in Fig. 1, apart from broadening the absorbing spectrum, the total reaction can get improved through the synergistic effect of photothermal combination: enhancing interfacial electron transformation [31], activating pyroelectric effect [32], driving gradient H migration [33], lowering the energy barrier of reaction [34] and accelerating the transportation of product [35].

For example, Zhang *et al.* [36] constructed a physical model of carrier spatial distribution and predicted its photoelectric performance to solve the problem of carrier generation and collection in oxide optoelectronic devices. They proposed a multi-field coupling mechanism of photothermal-electricity, and used the thermoelectric potential generated by photothermal generation to regulate the carrier transport characteristics. Through carrier dynamics analysis, including the analysis of carrier collection efficiency driven by temperature difference and the analysis of transient absorption spectrum, they found that the temperature difference potential can break the limitation of external auxiliary voltage, accel-

* Corresponding author.
E-mail address: wanglonglu@njupt.edu.cn (L. Wang).

https://doi.org/10.1016/j.cclet.2023.108513
1001-8417/

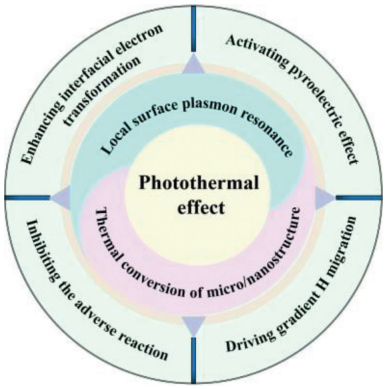

Fig. 1. Schematic illustration of the functions of photothermal effect.

erate carrier separation, inhibit recombination, prolong carrier lifetime, and finally improve the performance of the photoelectrode.

In this review, we first introduce the two main originations of photothermal effect, including local surface plasmon resonance (LSPR) and thermal conversion of micro/nanostructure. Subsequently, we discuss the destinations of heat from the view of catalytic reaction. (*i.e.*, enhancing interfacial electron transformation, activating pyroelectric effect, driving gradient H migration, inhabiting adverse reaction). Furthermore, we demonstrated a novel water vapor splitting to improve the whole catalytic system from the phase perspective and extend the bi-phase system to the electrolytic HER system. Last but not least, the challenges and outlooks of the photothermal H_2 evolution are presented. We hope to shed light on the conceptions and research progress of photothermal HER and provide ideas for the design and potential applications in this area.

2. Design of photothermal effect

Photothermal effect has been observed in different materials including inorganic materials (*e.g.*, plasmonic metals and semiconductors) [37,38] and organic materials (*e.g.*, polymers) [39]. However, in the reported HER processes, inorganic materials are most widely used and there are two main sources of heat widely employed in H_2 generation: local surface plasmon resonance and thermal conversion of micro/nanostructure. Local surface plasmon resonance derives from the coherent electron oscillations of the incident light and surface electrons [40]. The thermal conversion of photothermal materials (*e.g.*, black carbon-based materials, black silicon, black GaAs, and other black materials) can effectively increase the times of internal reflections, refractions, and scatterings within the nanostructures [41–43].

2.1. Local surface plasmon resonance

As widely reported, localized surface plasmon resonance would occur when the electric field oscillation of the incident light drives the collective oscillation of the free electrons distributed in certain regions on the surface of the material. The hot electrons of a higher energy level which only have a limited lifetime will achieve the conversion of energy form through electron–electron and electron–phonon scatterings and then dissipate the absorbed energy through phonon–phonon relaxation process [44]. Hence, three procedures of LSPR can be concluded as enhancement of local electric field, generation of hot electrons and photothermal conversion. Plasmonic metal nanoparticles, metallic oxides/nitrides, black polymers and carbon based materials which have quantities of free electrons within the molecules, have been reported existing LSPR [45]. Moreover, the absorption spectrum of LSPR can be tuned by controlling the size, shape, component of the material [46]. More applications of LSPR have been discovered from recent researches. Wu *et al.* [47] found that in the visible-near infrared region, the hot surface plasmon induced by LSPR effect can enhance the electrocatalytic activity of MXene. Yang *et al.* [48] reported that LSPR can significantly changes the selectivity of the reaction. Lu *et al.* [49] reported that hot plasmon induced by LSPR can move at a high speed to facilitate the catalytic activity of photocatalyst.

2.1.1. Local surface plasmon resonance of metallic oxide

Although many intrinsic metal compounds have photocatalytic properties, they do not have enough active sites due to their inert substrates, which greatly limit their catalytic efficiency. Active sites are often regulated by doping and defect engineering, among which oxygen doping is a common modification method [50–58]. Due to the difference of its radius and electronegativity, oxygen doping changes the band gap and regulates the activity of the base surface, thus providing enough free charges on the surface of material [45].

Our group [59] developed a oxide-MoS_2 through a defect-driven oxidation routine. O-doping strategy applied to MoS_2 can form molybdenum oxides on its surface, where abundant free charges can induce local surface plasmon resonance effect. As shown in Fig. 2a, driven by the electromagnetic field generated by the incident light, the freely movable charges oscillate at a certain frequency parallel. The oscillation is only limited to local regions because the size of nano material is much smaller than the wavelength of light. The product had a good photothermal performance, which can be found in Fig. 2b. Under the illumination of 808 nm, 1 W/cm^2 laser beam, the maximum temperature of can reach 54 °C. However, the oxidation degree of MoS_2 can affect the H_2 evolution results. Figs. 2c and d shows that the oxide-MoS_2 has the best H_2 evolution yields and the highest production rate (7.85 mmol g^{-1} h^{-1}). But the defective MoS_2 and the over-oxidation MoS_2 had relatively low production similar to 2H-MoS_2, which can be respectively attributed to poor surface electrons and destroyed molecular structure. As depicted in Fig. 2e, eosin Y (EY) excited to singlet state and finally become EY^{3*} through inter-system crossover. The triple excited state EY react with electron donator triethanolamine (TEOA). TEOA subsequently lose an electron and become $TEOA^+$ while EY^{3*} transform into EY^-. The highly reduced EY^- can transfer electrons to the surface of oxide-MoS_2 for HER. Meanwhile, oxide-MoS_2 can absorb light in 700 and 1000 nm to achieve photothermal conversion through LSPR effect. The reaction temperature increased and the HER efficiency was improved.

2.1.2. Local surface plasmon resonance of metallic particle

Metallic plasmonic particles like gold, silver, aluminum and platinum nanoparticles have a high density of free electrons which means LSPR can occur after absorbing the resonant light.

Gao *et al.* [45] designed a photothermal catalytic (PTC) gel composed by TiO_2/Ag nanofibers (NFs) and strong water absorber chitosan polymer (Fig. 3a). As shown in Fig. 3b, the gel structure can avoid light shielding of the upper catalyst in traditional suspension system and have a deeper light penetration depth. Moreover, the co-catalyst Ag NFs can heat the system which can both boost the catalytic reaction and accelerate the mass transport of H_2 gas. Results shows that, the co-catalyst Ag can greatly enhance light absorption from 400 to 800 nm (Fig. 3c). Furthermore, compared with other materials, TiO_2/Ag NFs and the PTC gel achieve an over 90% absorption of the whole solar spectrum (Fig. 3d). From the result shown in Fig. 3e, single TiO_2 NFs barely had HER performance, but after fabricating Ag with TiO_2 NFs, the HER performance got hugely improved from 50 μmol h^{-1} g^{-1} (TiO_2 NFs) to 1734 μmol h^{-1} g^{-1} under UV light and an enormous enhancement to 8580 μmol h^{-1} g^{-1} under visible-NIR light. The mechanism depi-

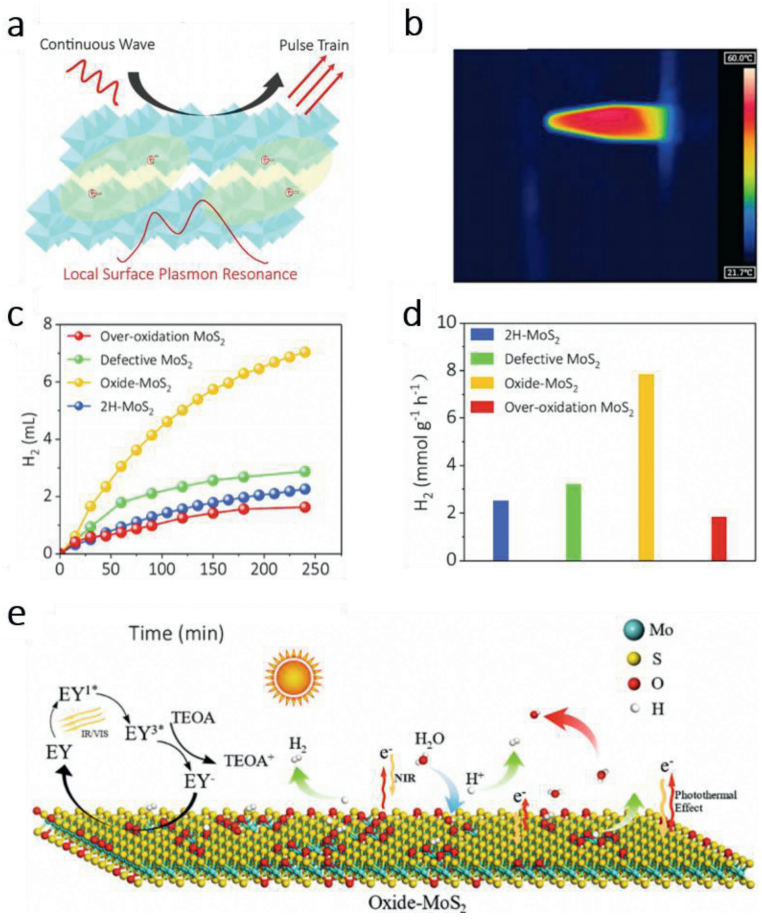

Fig. 2. (a) Schematic diagram of local surface plasmon resonance of MoS_xO_y. (b) Schematic of side-view infrared thermal image of the MoS_2 samples. Laser beam: 808 nm, 1 W/cm^2. (c) and (d) Comparison of PHER activities over 2H-MoS_2/EY (This sample refers to the perfect MoS_2 that prepared by hydrothermal synthesis at 220 °C), defective MoS_2, oxide-MoS_2, and over-oxidation MoS_2 under xenon lamp. (e) Mechanisms of PHER with oxide-MoS_2 as catalyst. Copied with permission [59]. Copyright 2022, Elsevier.

cted in Fig. 3f can be explained as, the UV excited electrons can be trapped by Ag particles for HER. Apart from boosting charge separation, LSPR effect of co-catalyst Ag particles can increase local temperature by absorbing solar light of lower energy, thus accelerating the reaction kinetics.

Additionally, Lu *et al.* [49] demonstrated that the LSPR effect of gold nanoparticles can be directly used to improve the rate and efficiency of electrochemical conversion. Using the electrocatalytic oxidation of glucose as a model system, the change of electrocatalytic performance of gold nanoparticles under LSPR excitation was systematically studied. The correlation between the electrocatalytic activity of glucose and the light intensity and wavelength was investigated. It was revealed that the thermal electron-hole generated by gold nanoparticles under LSPR excitation was the essential reason for the enhancement of the electrocatalytic activity. The mechanism of LSPR direct plasmonic accelerated electrochemistry reaction (PAER) was proposed by using single particle dark field microscopy spectroscopy and electrochemistry. This work reveals the electrochemical reaction mechanism based on the enhanced LSPR effect of noble metal nanoparticles, and provides a new idea for the design of a new electrochemical energy conversion device and the construction of electrical analysis devices using the local surface plasmon resonance effect.

2.2. Thermal conversion of micro/nanostructure

For bulk materials, low emissivity is one of the obstacles limiting light harvesting capacity [60]. The construction of micro/nanostructure in black carbon-based materials, black silicon, black GaAs, and other black materials help achieve a high solar-to-heat conversion rate by changing the intrinsic reflectance of materials and inducing refraction and scattering inside the materials [61]. When the dimension of the structures matches the wavelength of the incident light, the refractive properties of the material will change [62]. Light can be trapped in the structures and subsequently absorbed by multiple internal reflection. Aligned [63,64], porous [65,66], hierarchical [67] or other spatial structures have been developed for better light harvesting performance.

Li *et al.* [68] constructed a C@TiO_2/TiO_{2-x} ternary spatial junction nanoreactor with yolk-shell (YS) structure. YS structure can effectively reduce heat loss and minimize the transmission distance of photogenerated carriers. As shown in Figs. 4a and b, the hydrogen evolution performance of C@TiO_2/TiO_{2-x} was the most outstanding compared with all the precursors in both photocatalysis or photothermal catalysis. Moreover, the catalytic activity of the whole reactor is basically unchanged after 5 tests, showing strong stability (Fig. 4c). The construction of homojunction can form a Ti-O-C tunnel allowing charge transmission between carbon sphere (CS) and TiO_2, while heterojunctions can form internal electric field due to Fermi level difference between the two interfaces (Figs. 4d–f).

The mechanism is further elaborated in Fig. 4g. CS, TiO_2 and TiO_{2-X} are photoexcited to produce electron-hole pairs under the irradiation of sunlight. The electrons in the CS conduction band flow to the TiO_2 conduction band instantaneously through the Ti-O-C channel (charge transfer bridge), and further flow to the TiO_{2-X}

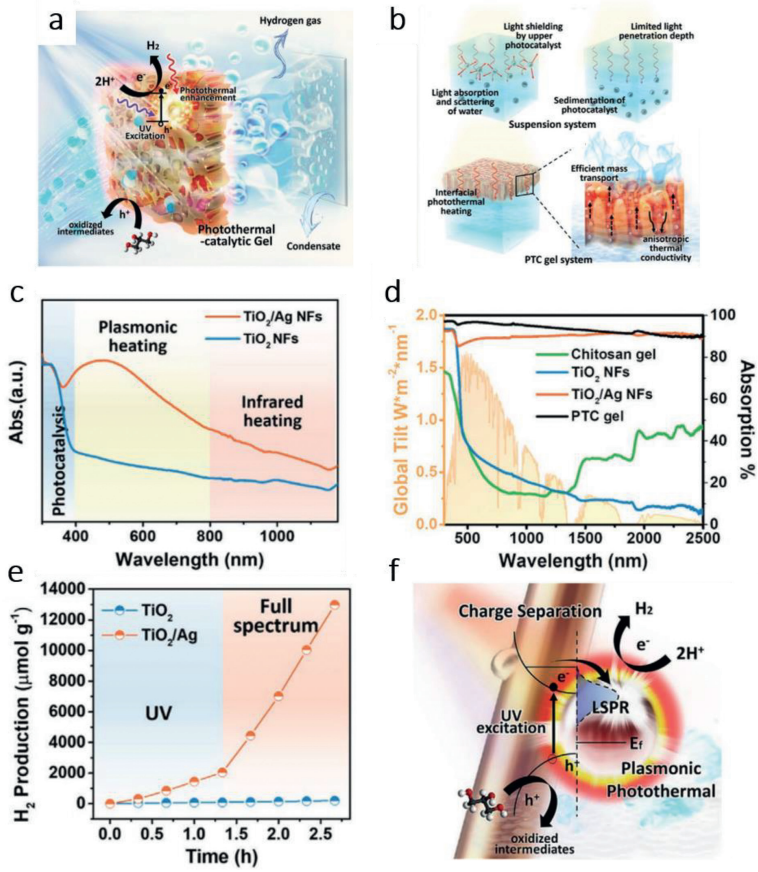

Fig. 3. (a) Schematic drawing of the designed PTC gel for concurrent solar vaporization and hydrogen generation. (b) Inefficient light utilization in the suspension system. Inactive nanomaterials caused by sedimentation and light penetration. Interfacial photothermal heating of PTC Gel. Efficient mass transport and light absorption through the aligned pores within the PTC gel. (c) Absorption spectra of TiO_2 NFs and TiO_2/Ag NFs. (d) Calculated absorption spectra of TiO_2 NFs, TiO_2/Ag NFs, chitosan gel, PTC gel, and spectral solar irradiance (AM 1.5). (e) Hydrogen generation by TiO_2 NFs and TiO_2/Ag NFs in glycerol–water solution under both UV light and full spectrum irradiation. (f) Schematic diagram of the proposed mechanism of plasmonic photothermal enhanced catalysis. Copied with persmission [45]. Copyright 2020, Wiley Online Library.

conduction band under the action of the internal electric field. H^+ is reduced to H_2 by the heat generated by the photothermal effect of carbon core. At the same time, the valence band h^+ of TiO_2 migrates to the valence band of CS and reacts with the sacrificial reagent (TEOA). However, due to the repulsive force of the internal electric field, the photogenerated holes on the VB of TiO_2 cannot be transferred to the TiO_{2-X}, effectively separating the e^- and h^+ generated on TiO_2, and finally achieving effective charge separation under the condition of efficient photothermal conversion. It provides the basis for rational design of high-performance carbon-semiconductor hybrids in multi-electronic water reduction.

3. Various functions of photothermal effect

Above mentioned are different mechanisms of solar-to-heat conversion of different photothermal materials. However, heat from these different sources plays a totally different role in HER process [69]. Heat has one or hybrid functions in each different photothermal catalytic system [70,71]. Therefore, it is meaningful to summarize the basic functions of photothermal effect for better understanding of the photothermal H_2 evolution system. Herein, we conclude some basic functions of photothermal effects: enhancing interfacial electron transformation [72], activating pyroelectric effect [73,74], driving gradient H migration [33].

3.1. Enhancing interfacial electron transformation

According to the principle of photocatalysis, the migration path of electrons excited by incident light is valence band-conduction band-active sites on the surface [75,76]. So, the rate of migration is decisive to the catalytic performance [77,78]. Therefore, the photothermal effect can accelerate the targeted migration of electrons by accelerating the reaction kinetics in the system [79].

Tang *et al.* [31] fixed CdS nanoparticles on the surface of Vs-1T-WS_2 nanoflowers through a solvothermal method. As shown in Fig. 5a, single CdS NPs or Vs-1T-WS_2 would not catalyze the whole HER process. But after coupling both two materials, H_2 was able to be generated by the whole catalytic system. It was noteworthy that, the mass fraction of Vs-1T-WS_2 would affect the production rate of H_2 and Vs-$1T_{0.15}$-WCS had the best performance among all the obtained products. Under the irradiation of visible light, photothermal effect by auxiliary catalyst Vs-1T-WS_2 would help enhance the HER performance and Vs-$1T_{0.15}$-WCS had the best photothermal property compared with $Pt_{0.02}$-CdS, CdS and Vs-1T-WS_2 (Fig. 5b). Employing Vs-$1T_{0.15}$-WCS to assess the best incident light condition, the best performance of 81.2 mmol g^{-1} h^{-1} was detected under simulated sunlight (AM 1.5), which was ascribed to the simultaneous excitation of the photothermal effect and inter-band transition of the charges at the interface (Fig. 5c). They further calculated the Gibbs free energy of hydrogen adsorption in different catalysts and result showed that Vs-1T-WCS had the lowest reaction energy barrier, which proved that the Vs of Vs-1T-WS_2 was easier to adsorb *H (Fig. 5d).

The researchers revealed the mechanism as the synergistic effect of electron modulation and photothermal effect (Figs. 5e–g). The tight contact of the Vs-1T-WS_2 and CdS gives rise to the relocation of the elections near the heterogeneous interface thus resulting in the energy band of CdS bending down to a lower level.

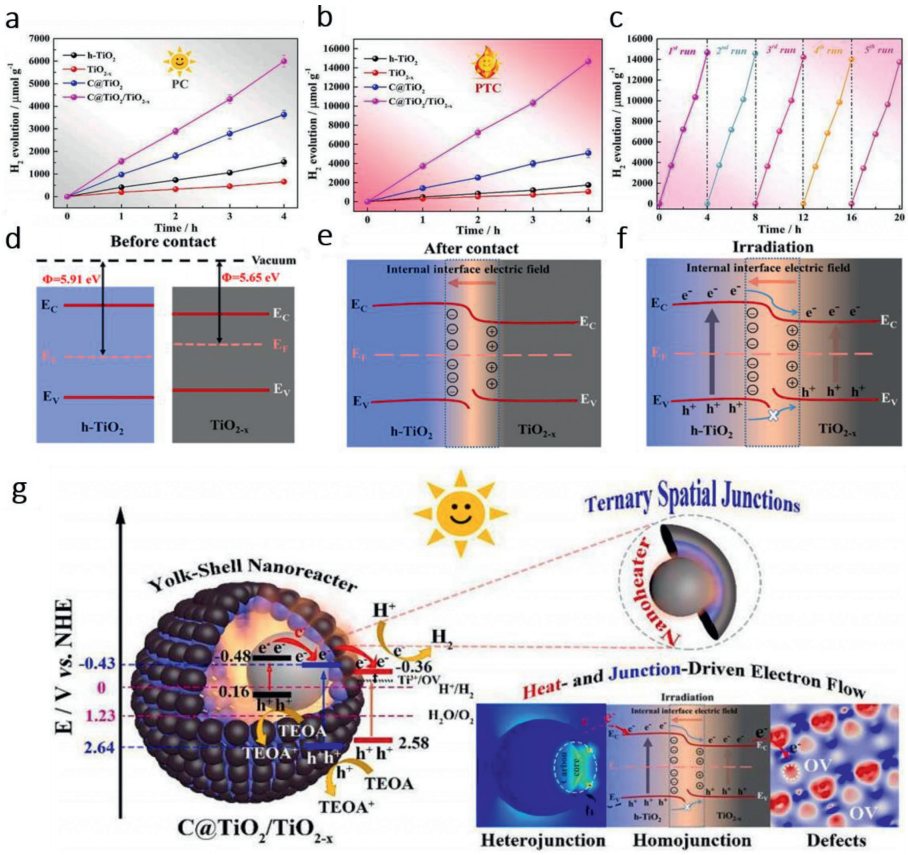

Fig. 4. Photocatalytic and photo-thermal catalytic hydrogen evolution reaction performances of C@TiO_2/TiO_{2-x} yolk–shell (YS) nanoreactor. Hydrogen generation profiles in (a) photocatalytic (ambient temperature) and (b) photo-thermal catalytic (without control temperature) over different catalysts (without co-catalyst Pt) under simulated sunlight illumination. (c) Recycling tests of photo-thermal catalytic H_2 evolution of C@TiO_2/TiO_{2-x}. (d-f) Sketches of internal electric field and charge transfer. (g) Illustration of the possible transfer process of the photogenerated electrons (e^-) and holes (h^+) in C@TiO_2/TiO_{2-x} YS nanoreactor and the photo-thermal catalytic mechanism for enhanced H_2 evolution under simulated sunlight (AM 1.5 G) irradiation. Copied with permission [68]. Copyright 2021, Elsevier.

As a result, a build-in electric field is formed from Vs-1T-WS_2 to CdS. Under the irradiation of visible light, the photogenerated electrons from CdS migrate directly to S vacancies which were primarily the adsorption sites of *H primarily. Meanwhile, the photothermal effect of the S vacancies greatly enhances the interfacial transformation of the electrons, which is the main driving force of the hydrogen evolution process.

The new catalyst achieved a hydrogen evolution rate of 70.9 mmol g^{-1} h^{-1} at 500 nm and an apparent quantum yield (AQY) of 39.1% and provided the possibility for non-precious metal co-catalysts for hydrogen evolution.

3.2. Activating pyroelectric effect

The pyroelectric effect can form charges by temperature oscillation-dependent spontaneous polarization [80–82]. The charges originate from the thermal gradient can participate in the catalytic reaction [83] and form inner electric field to act as a driving force to govern the directional migration of photogenerated carriers which will promote the separation of carriers [38].

Huang *et al.* [84] coated three-dimensional hierarchically structured coral-like $BaTiO_3$ NPs with *in situ* grown Au NPs to construct a catalytic system with synthetic effect mentioned above. As shown in Figs. 6a and b, the HRTEM and HAADF-STEM image showed that the characteristic lattice fringes agrees with the D-spacings of $(0\bar{1}1)$, (100), $(\bar{1}1\bar{1})$ in $BaTiO_3$ and $(\bar{1}1\bar{1})$, $(\bar{1}\bar{1}1)$, (200) in Au, which meant the Au particles grew well on the surface and did not destroy the structure of $BaTiO_3$. Fig. 6c showed the temperature distribution of the system, from which we can find that the contact region of Au NPs and W-$BaTiO_3$ can reach over 300 °C. Compared with single $BaTiO_3$ NPs and Au NPs, the HER performance got greatly improved, which proves that the HER performance derives from the synergistic effect of $BaTiO_3$ and Au (Fig. 6d). Moreover, the nanosecond incident light was sorted to be the best light source of the catalytic system because its rapid change of temperature gradients (Fig. 6e). The mechanism of the total reaction is shown in Fig. 6f. The well contact Au particle heats the contact surface of $BaTiO_3$ through its LSPR effect and activates the pyroelectric effect. During the thermal cycle the uncompensated pyroelectric surface charges will participate in the water splitting process. Moreover, the internal electric field built up from the surface pyroelectric charges can further facilitate the charge separation and charge transfer for pyro-catalytic hydrogen and oxygen production.

3.3. Driving gradient H migration

Unwanted random electron-hole recombination occurring in charge flow can lead to low conversion efficiency for hydrogen evolution [85–87]. Surface and interior modification has been regarded as an effective way to improve charge separation efficiency for photocatalysts [88,89]. It is reported that construction of self-adapting vacancies by heteroatom doping can separate carriers effectively in a desired route [90–96]. Therefore, controllable vacancy generation induced by accurate atomic doping or substitution is a feasible way to improve catalytic performance.

In this regard, it was reported that activated hydrogen atoms could migrate from a metal particle to the catalyst support on

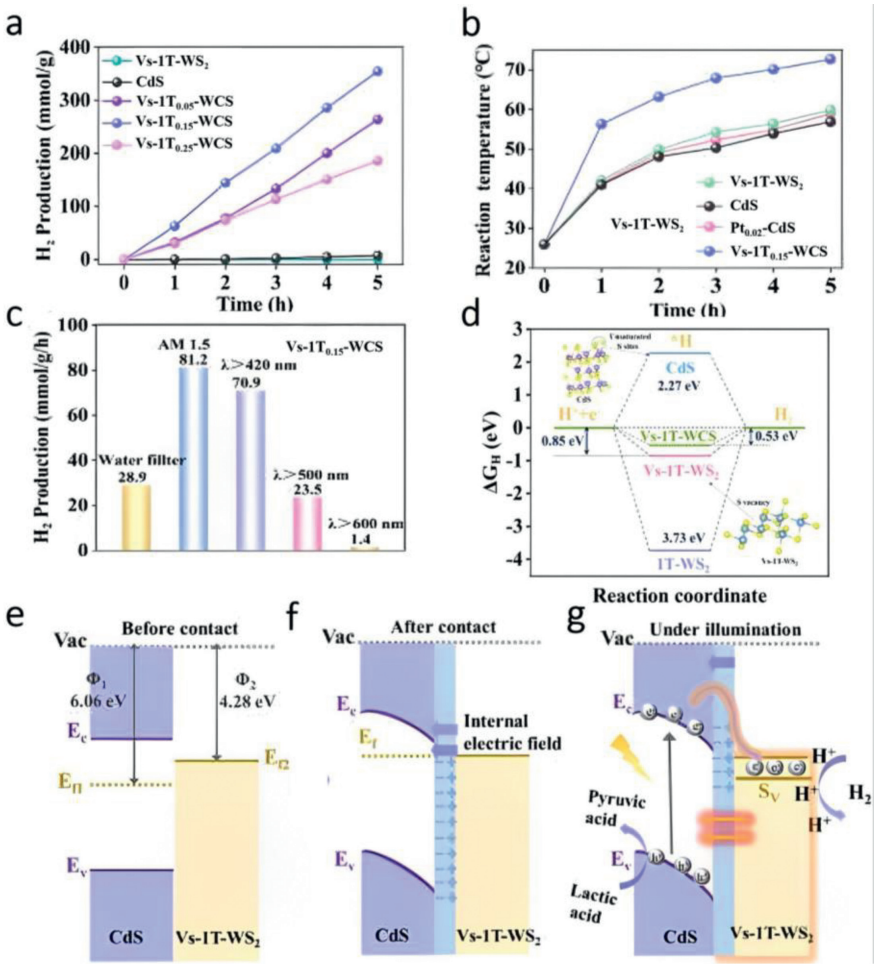

Fig. 5. (a) H_2 evolution amount of Vs-1T-WS_2, CdS and Vs-1T-WCS at different irradiation time. (b) Reaction temperatures of photocatalytic hydrogen precipitation reaction systems with different catalysts. (c) Photocatalytic hydrogen evolution performance of Vs-1$T_{0.15}$-WCS under different wavelengths of light irradiation. (d) ΔG_H of the prepared catalysts (the calculated sites of CdS were at the edge of the unsaturated S atom and the calculated sites of Vs-1T-WS_2 were at the S vacancies site). (e-g) Schematic diagram of the energy band structure and photocatalytic hydrogen precipitation of Vs-1T-WCS. Copied with permission [31]. Copyright 2022, Elsevier.

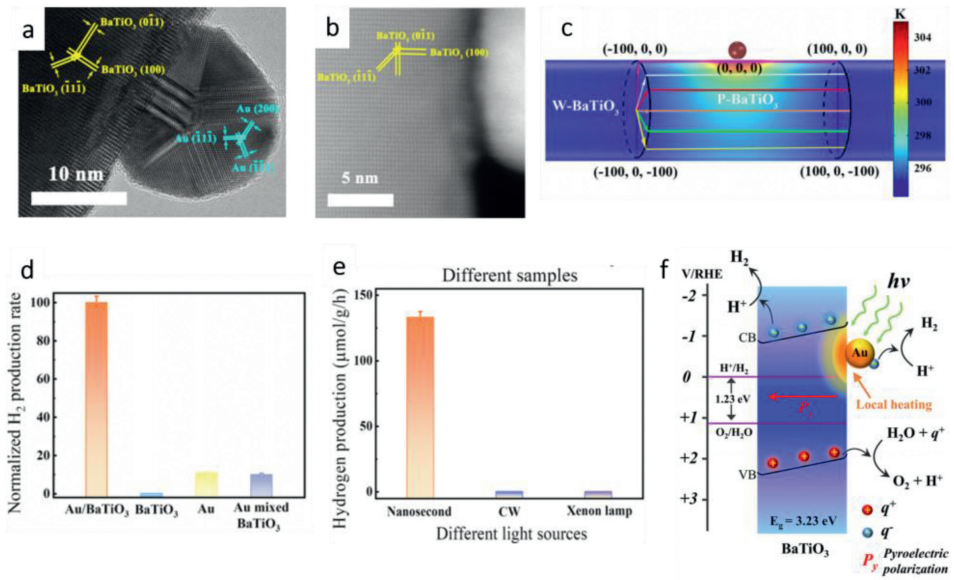

Fig. 6. (a) HRTEM image. (b) HAADF-STEM image with atomic structure as inset. (c) Temperature distribution of the structural model of a Au NP (9 nm in radius) suspending over a $BaTiO_3$ cylinder with length of 1 μm and radius of 50 nm at the moment with highest temperature inside Au NP. (d) H_2 generation by Au/$BaTiO_3$ NPs illuminated under different light sources. (e) Normalized H_2 production rate (normalized to the production rate of Au/$BaTiO_3$ NPs) of different samples under the irradiation by a 532 nm nanosecond laser. (f) Schematic illustration of pyro-catalytic hydrogen generation of Au/$BaTiO_3$ NP driven by surface plasmon local heating. Copied with permission [84]. Copyright 2022, Nature Publishing Group.

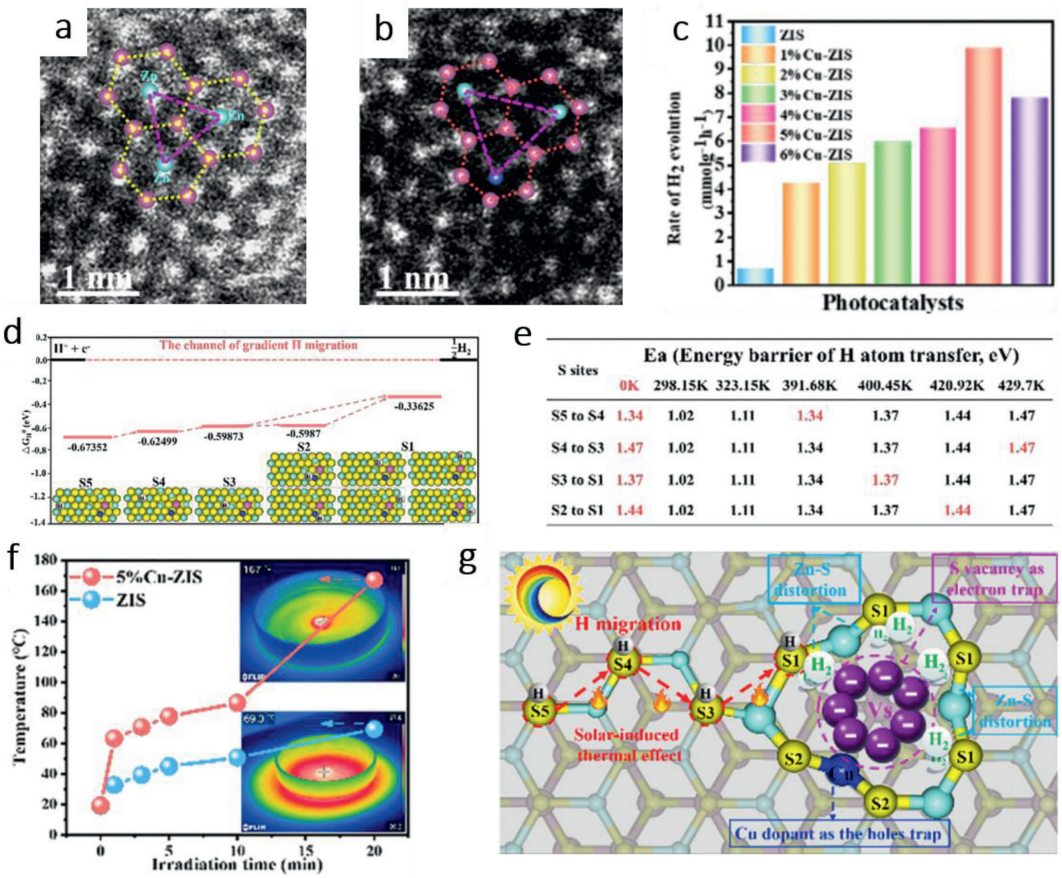

Fig. 7. (a) and (b) HAADF-HRSTEM image of 5% Cu-ZIS. (c) photocatalytic H_2 evolution rate of ZIS and xCu-ZIS (x = 1%–6%). (d) Adsorption free energy of H ($\Delta G_H{}^0$) of different S sites and H gradient migration. (e) Energy barrier of H atom migration (E_a, eV) at different temperatures between different S sites. (f) The temperature variation of ZIS and 5% Cu-ZIS with increasing irradiation time. (g) Schematic illustration of gradient H migration for H_2 evolution on Zn facet over Cu−ZIS. Copied with permission [33]. Copyright 2021, American Chemical Society.

the surface though the heterogeneous interface because of hydrogen spillover [97,98]. Hence, it is viable to construct gradient active sites to migrate H atoms from hydrogen-abundant sites to hydrogen-scant sites. In this process, the heat can lower the energy barrier of the migration and accelerate the migration kinetics.

Zhang *et al.* [33] fabricated a copper-doped $ZnIn_2S_4$ nanosheet with self-adapting S vacancy. As shown in Figs. 7a and b, after Cu atom substituting the Zn atom, self-adapting Vs will appear because of different chemical bond lengths of Cu-S and Zn-S, namely Jahn-Teller distortion. The generated S vacancies will construct a gradient channel for H migration and H_2 evolution. It was found that the density of doped Cu atoms could boost H_2 generation, but excess doping of Cu would result in a decrease of H_2 production rate because the formation of CuS become recombination sites of photogenerated charges (Fig. 7c). The optimal density of copper dopants is 5%. Shown in Fig. 7d, the route of H migration consists of 5 gradient active sites (S5-S1) with gradually lower reacting energy barriers. Moreover, with the rise of the temperature, the energy barrier of H atom transfer will decrease, making it easier for H atoms to migrate to a more suitable site for HER (Fig. 7e). Intriguingly, S2 active site will be eliminated from the ultimate migration path because of the energy barrier of S3-S1 is lower than that of S2-S1 at 0 K. Furthermore, the temperature of 5% Cu-ZIS can reach 167 °C within 20 min, which shows a more excellent photothermal effect than ZIS (69.3 °C) (Fig. 7f). The mechanism of the whole system can be concluded in Fig. 7g. The accumulated heat can drive the migration of H atom along the route S5-S4-S3-S1 and the trapped H atoms will gather to generate H_2 at S vacancies. Ultimately, 5% Cu-ZIS achieves optimum photo-catalytic hydrogen evolution activity of 9.8647 mmol g^{-1} h^{-1}, which is 14.8 times higher than 0.6640 mmol g^{-1} h^{-1} for $ZnIn_2S_4$, and apparent quantum efficiency reaches 37.11% at 420 nm.

3.4. Inhibiting the adverse reaction

In water splitting reaction, the generated oxygen and hydrogen can react at the active sites to generate water reversely [99–101]. The competition between hydrogen–oxygen production ($2H_2O \rightarrow 2H_2 + O_2$) and hydrogen–oxygen recombination ($2H_2O \leftarrow 2H_2 + O_2$) is unfavorable and will leads to a low solar-to-hydrogen (STH) efficiency [102,103]. Recently, evidence has been found that the intensity of adverse reactions is adjustable by controlling the temperature.

Zhou *et al.* [104] reported that proper temperature can inhibit the reverse reaction. Fig. 8a shows the catalytic system of rhodium (Rh)/chromium oxide (Cr_2O_3)/cobalt oxide (Co_3O_4)-loaded InGaN/GaN NWs. From the element mapping of the catalyst shown in Fig. 8b, Rh, Cr_2O_3 and Co_3O_4 only distribute on the surface of the catalyst while the internal part is filled with InGaN and GaN. They first designed a temperature-controllable photocatalytic system to perform overall water splitting (OWS) in pure water at different temperatures ranging from 30 °C to 80 °C under the same concentrated simulated solar light (3800 mW/cm^2). The result showed the significant improvement of the STH efficiency with the rise of temperature (Fig. 8c). They further confirmed the mechanism behind the promotional effect of heat in the catalytic re-

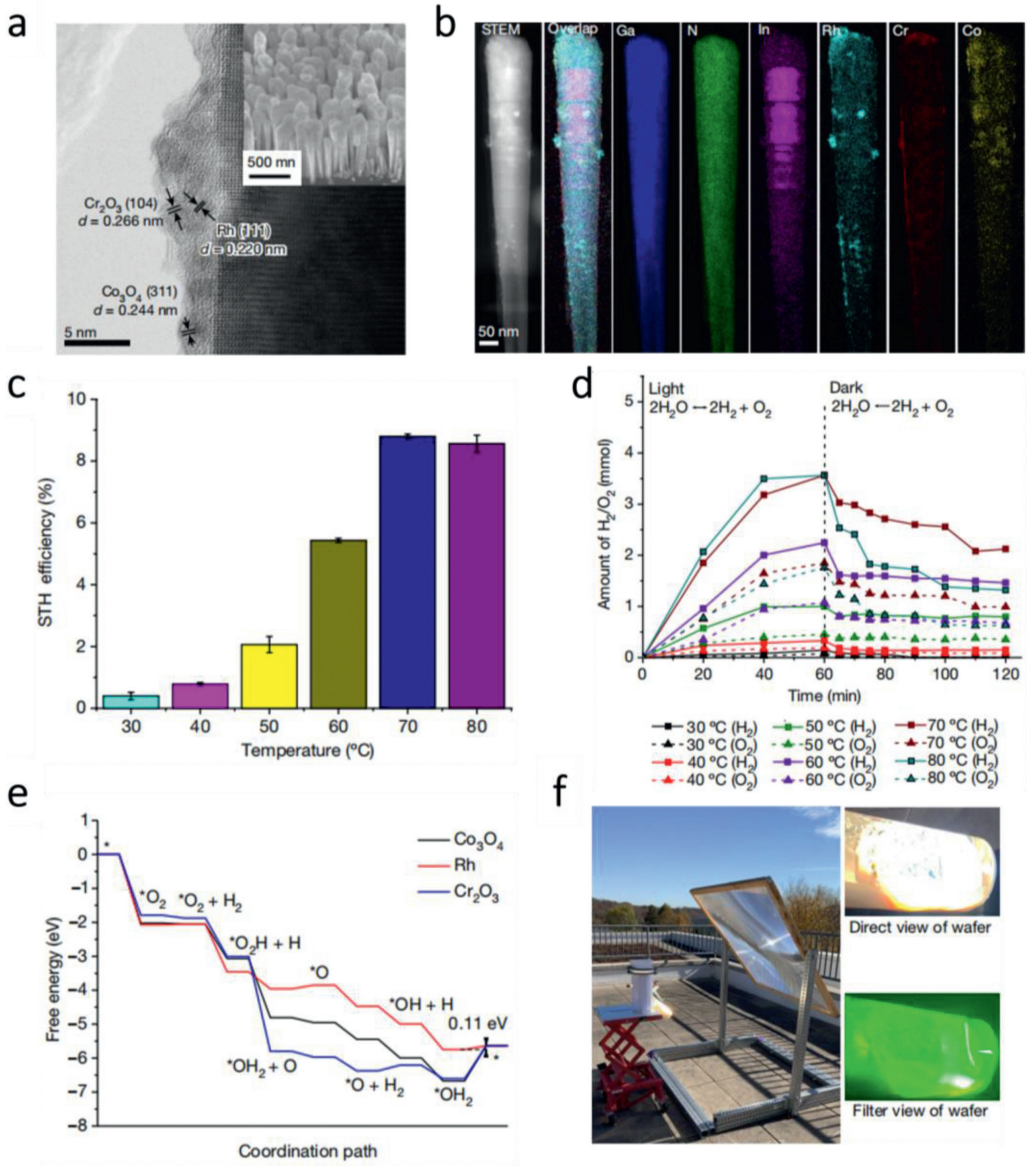

Fig. 8. (a) HRTEM of the supported Rh/Cr_2O_3/Co_3O_4 cocatalyst on the InGaN/GaN NWs. Inset: FESEM of the Rh/Cr_2O_3/Co_3O_4-loaded InGaN/GaN NWs. (b) STEM and element mapping of the Rh/Cr_2O_3/Co_3O_4-loaded InGaN/GaN NWs. (c) Temperature dependent STH efficiency of the Rh/Cr_2O_3/Co_3O_4–InGaN/GaN NWs. A 300-W Xe lamp equipped with an AM1.5 G filter was used to produce concentrated light of 3800 mW/cm^2 on a 0.8 cm × 0.8 cm Rh/Cr_2O_3/Co_3O_4-loaded InGaN/GaN NW wafer. (d) Temperature-dependent hydrogen–oxygen recombination reaction. (e) Free-energy profile of hydrogen–oxygen recombination on the cocatalyst Co_3O_4, Rh and Cr_2O_3. (f) Image of outdoor photocatalytic OWS system on North Campus at the University of Michigan, Ann Arbor, Michigan, United States. Copied with permission [104]. Copyright 2023, the Nature Publishing Group.

action through a contrast test (Fig. 8d). Under the dark condition, photocatalyst was inhibited, the amount of H_2 and O_2 reduced by the ratio of 2:1 which directly confirm the existence of the hydrogen–oxygen recombination. Importantly, the balance content of H_2 and O_2 rise simultaneously with the temperature, which proved the inhibition effect of temperature on the adverse reaction. Interestingly, the gas amount decreased under 80 °C which can be attributed to accelerated the mass transfer in water caused by temperature increase. The free-energy profile can help further elucidate the mechanism of inhibition of adverse reaction by temperature (Fig. 8e). Calculations showed that the energy barrier (0.11 eV) of hydrogen–oxygen recombination on Rh was lower. Hence, Rh is the center for hydrogen–oxygen recombination. Since most steps except water desorption in the hydrogen–oxygen recombination on Rh were typically exothermal, it is acceptable to restrain the adverse reaction. The outdoor photocatalytic OWS system shown in Fig. 8f achieved a surprising average STH efficiency of 6.2% within 14 cycles. Their study broke the limit of photocatalytic water splitting and overcame the efficiency bottleneck of solar hydrogen production.

4. Photothermal catalytic bi-phase system

From the perspective of the catalytic reaction process, we have discussed varies functions of heat. However, catalytic reaction is only one of the crucial parts of the total HER process [105,106]. From the phase-interface perspective, most of the reported photocatalytic water splitting system adapt a tri-phase pattern, including solid catalyst, fluid water, gas hydrogen. Nevertheless, recent researches showed that the state of water is decisive to the HER performance [107,108]. By absorbing the heat from sunlight to convert liquid water into water vapor, and using it in photocatalysis

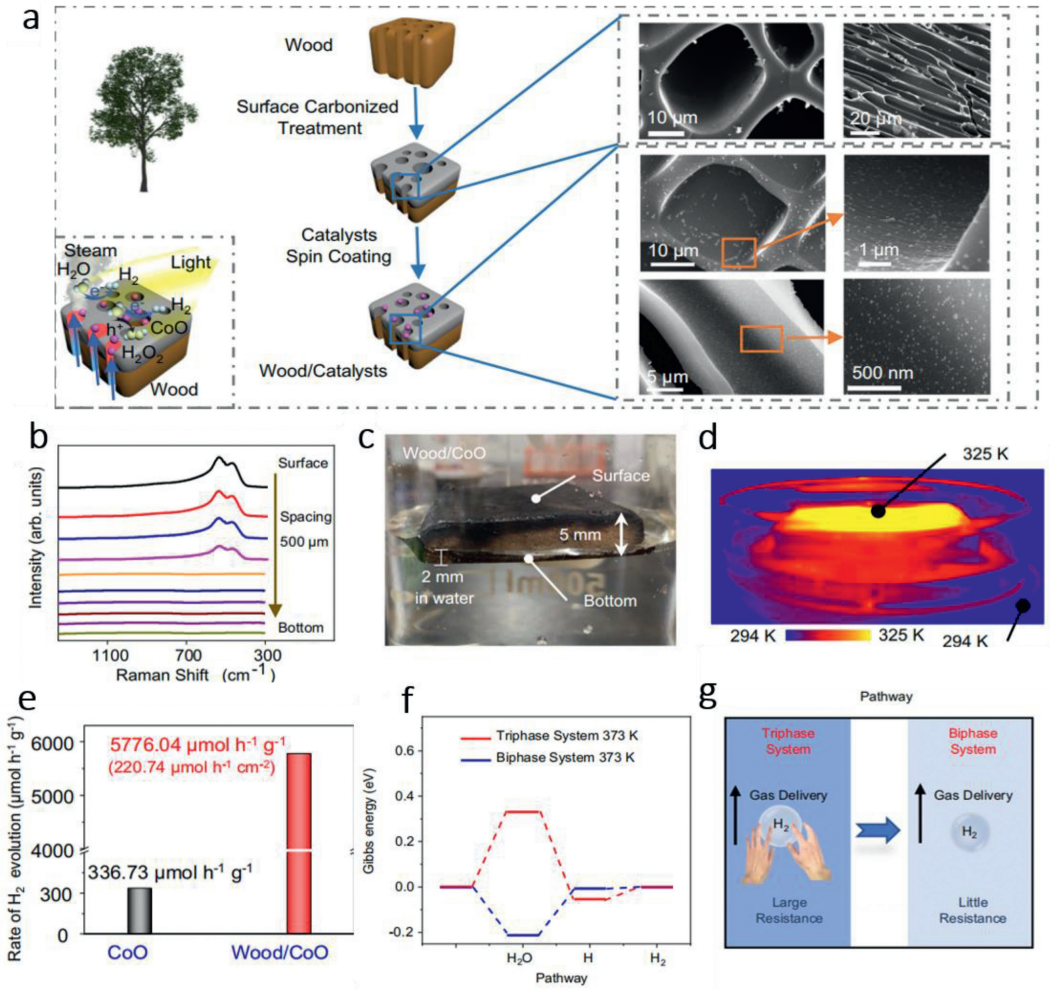

Fig. 9. (a) Schematic of the fabrication process of the wood/photocatalyst structure that generates the water steam and catalyzes its splitting for hydrogen evolution. (b) Raman spectra taken at different depths along the cross section of wood/CoO microchannels with an interval of 500 μm. (c) The photo of the wood/CoO system floating on water. (d) Infrared radiation thermal image from the wood/CoO system under light illumination. (e) Rate comparison of H_2 evolution in the tri-phase CoO NPs system and wood/CoO bi-phase photothermal–photocatalytic system (area: 7.85 cm^2, mass: 0.3 g). (f) Gibbs energy of a photocatalytic reaction in the tri-phase system (373 K) in comparison with the bi-phase system (373 K) over the pure CoO surface. The photocatalyst is CoO NPs. (g) Schematic of the hydrogen transport resistances in the liquid- and gas-phase environments. Copied with permission [35]. Copyright 2021, the Nature Publishing Group.

and electrocatalysis, the energy barrier of the reaction can be reduced and the transport speed of the product can be accelerated [109,110].

4.1. Photothermal photocatalytic bi-phase system

Many reports have confirmed the advantage of the construction of bi-phase system by doing contrast tests. For example, Han *et al.* [111] compared the H_2 production rate of the tri-phase and bi-phase TiO_2 catalytic system. The rate of the tri-phase system was 162.7 μmol m^{-2} h^{-1} while that of the bi-phase was 487.4 μmol m^{-2} h^{-1}, which proved the superiority of bi-phase system.

Li *et al.* [35] found that the stage of water makes a huge difference to H_2 evolution performance. They fabricated a bi-phase system constructed by carbonized wood slice with HER catalyst spin-coated on its surface (Fig. 9a). Raman spectra of the wood/CoO system showed that the thickness of the surface catalyst was about 2 mm and the actual measurement of the depth immersion in water of the wood was 2 mm, which proved that CoO did not contact directly with liquid water (Figs. 9b and c). Under the irradiation of solar light, the carbonized wood will be heated to a high temperature (Fig. 9d) and transform the liquid water into water vapor, known as the photothermal transpiration effect. Gas water can react directly with CoO NPs and generate H_2. As shown in Fig. 9e, the evolution rate of bi-phase system is about 17 times the rate of tri-phase system using CoO NPs only. DFT calculations were also implemented to give a quantitative analysis of the advantage of the bi-phase system. Results showed that gas water can greatly lower the energy gap of the water splitting process (Fig. 9f). Moreover, the stage change of water makes the transmission resistance of H_2 shrink 2 orders of magnitude, thus achieving easier collection of H_2 (Fig. 9g).

4.2. Photothermal electrocatalytic bi-phase system

Introducing thermal factors to photocatalytic reactions has widely reported as a conducive method for hydrogen evolution. Similarly, introducing the bi-phase system to electrocatalytic water splitting may improve the performance of water electrolysis, which is rarely reported [112,113]. The total reaction can be considered as a photothermal assisted electrolysis process.

Li *et al.* [114] developed the electrocatalytic reaction system by planting surface carbonized wood structure on the water and suspending the electrocatalytic device over the wood structure (Fig. 10a). As shown in Fig. 10b, they assembled the whole catalytic system. Under the illumination of solar light, the carbonized wood

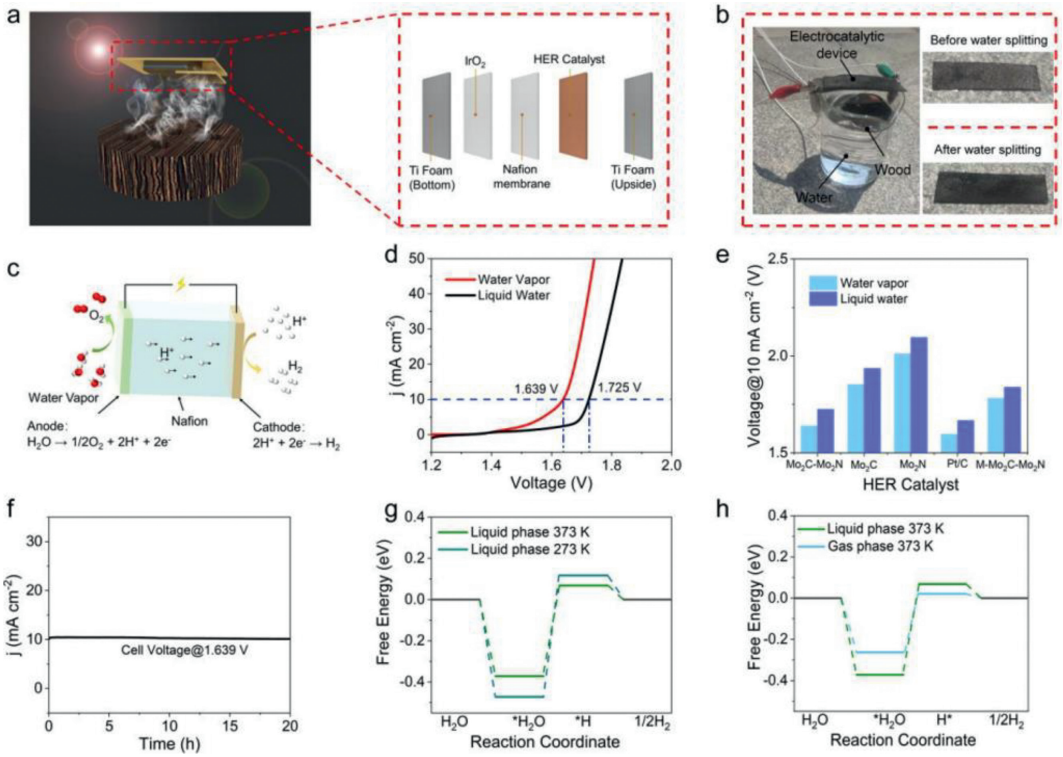

Fig. 10. (a) The diagrammatic sketch of the electrocatalytic water vapor splitting device based on the wood structure, the inset is the schematic illustration of the electrocatalytic water vapor splitting device configuration. (b) Photograph of the setup for the electrocatalytic steam splitting, insets are the photographs of setup before and after water splitting. (c) Sketch of the mechanism of the water vapor splitting electrolyzer. (d) Polarization curves of electrolyzer adopting Mo_2C-Mo_2N heterostructures as HER electrocatalyst at a scan rate of 5 mV/s in the vapor phase and liquid phase, respectively. (e) Summaries of the voltage at 10 mA/cm^2 using the Mo_2C-Mo_2N, Mo_2C, Mo_2N, M-Mo_2C-Mo_2N and 20 wt% Pt/C as HER electrocatalyst in the liquid water and water vapor. (f) Chronoamperometry curve of Mo_2C-Mo_2N heterostructures at a voltage of 1.639 V in the water vapor. (g) Free energy profiles of Mo_2C-Mo_2N heterostructures under different temperatures. (h) Free energy profiles of Mo_2C-Mo_2N heterostructures under different phase states. Copied with permission [114]. Copyright 2022, Wiley Online Library.

will transform liquid water into water vapor through photothermal transpiration effect. The generated water vapor will contact directly with the electrocatalytic device and will be electrolyzed by the poles which are commonly used in traditional water electrolysis. The reacting process is totally changed compared with the electrolysis of liquid water shown in Fig. 10c. The novel photothermal assisted electrocatalytic device greatly improves the performance of water electrolysis. Lower bios voltage is needed to support the whole process (Fig. 10d). The same conclusion can be drawn using different HER catalysts (Fig. 10e). Furthermore, we can find that traditional Pt/C catalyst displayed the best catalytic performance, while the Mo_2C-Mo_2N catalyst they developed performed second only to the Pt/C catalyst.

The stability of the system is also desirable. As shown in Fig. 10f, the function remained barely unchanged during the 20 h reaction. Moreover, density functional theory (DFT) calculations were implemented to further analyze the reaction. The results showed that higher temperature can lower the energy barrier of water splitting process (Fig. 10g). Furthermore, under the same temperature, the reaction energy barrier of gas stage water electrolysis is apparently lower than liquid stage water, which verifies the above-mentioned conclusion from another dimension (Fig. 10h). Li's work opened a new gate for introducing photothermal effect to electrocatalysis.

5. Challenges and outlooks

In recent decades, photothermal catalytic system is gradually mature and has become a research hotspot in the field of new energy. All above, we conclude the mechanisms and applications of photothermal effect mentioned in recent researches. However, this fast-growing research field still face severe challenges [115–117]. Firstly, the source of heat for hydrogen production by photothermal catalysis is still limited. Although many photothermal methods are reported, the methods that can be used for hydrogen production are very limited. Secondly, most of the researches on photothermal effect are implemented in photocatalytic hydrogen evolution system, but the researches on photothermal effect in other catalytic systems (such as electrocatalysis) are not widely reported. Thirdly, most reports focus on improving catalytic performance from the perspective of catalyst, but few of them study the regulation of the overall catalytic system. Since catalyst is only one of the decisive parts in the whole system, effective ways to improve the performance can be found from other angles. Last, the systems with good catalytic performance are rather complex, of which the preparation conditions are strict and the cost is high, so it is difficult to achieve industrial production. We hope that future studies can further explore the above problems, improve the theoretical system of photothermal catalytic hydrogen production, and put forward feasible industrial production programs. These years have witnessed the huge leap of new energy, but a long tough journey is just in front of us.

Declaration of competing interest

We declare that we have no financial and personal relationships with other people or organizations that can inappropriately influence our work, there is no professional or other personal interest of any nature or kind in any product, service and/or company that could be construed as influencing the position presented in, or the review of, the manuscript entitled.

Acknowledgments

This work was financially supported by the Natural Science Foundation of China (No. 51902101), Natural Science Foundation of Jiangsu Province (No. BK20201381), Science Foundation of Nanjing University of Posts and Telecommunications (No. NY219144), Postgraduate Research & Practice Innovation Program of Jiangsu Province (No. SJCX22_0254).

References

[1] Y. Li, X. Bai, D. Yuan, et al., Nat. Commun. 13 (2022) 776.
[2] H. Ahmad, S.K. Kamarudin, L.J. Minggu, et al., Renew. Sustain. Energy Rev. 43 (2015) 599–610.
[3] C.H. Liao, C.W. Huang, J.C.S. Wu, Catalysts 2 (2012) 490–516.
[4] M. Ni, M.K.H. Leung, D.Y.C. Leung, et al., Renew. Sustain. Energy Rev. 11 (2007) 401–425.
[5] M.R. Gholipour, C.T. Dinh, F. Beland, et al., Nanoscale 7 (2015) 8187–8208.
[6] X. Zou, Y. Zhang, Chem. Soc. Rev. 44 (2015) 5148–5180.
[7] B.A. Pinaud, J.D. Benck, L.C. Seitz, et al., Energy Environ. Sci. 6 (2013) 1983–2002.
[8] C.A. Rodriguez, M.A. Modestino, D. Psaltis, et al., Energy Environ. Sci. 7 (2014) 3828–3835.
[9] T. Hisatomi, K. Domen, Nat. Catal. 2 (2019) 387–399.
[10] A. Fujishima, K. Honda, Nature 238 (1972) 37–38.
[11] H. Irie, J. Ceram. Soc. Jpn. 130 (2022) 611–620.
[12] F. Meyer, P.S. Halasyamani, G. Masson, ACS Org. Inorg. Au 3 (2022) 1–3.
[13] A. Kobayashi, S. Takizawa, M. Hirahara, Coord. Chem. Rev. 467 (2022) 214624.
[14] H.S. Son, S.J. Lee, I.H. Cho, et al., Chemosphere 57 (2004) 309–317.
[15] K. Wenderich, G. Mul, Chem. Rev. 116 (2016) 14587–14619.
[16] A. Ajmal, I. Majeed, R.N. Malik, et al., RSC Adv. 4 (2014) 37003–37026.
[17] A.M. Al-Hamdi, U. Rinner, M. Sillanpää, Process Saf. Environ. Prot. 107 (2017) 190–205.
[18] S. Zhang, RSC Adv. 4 (2014) 15835–15840.
[19] J. Zhang, X. Jin, P.I. Morales-Guzman, et al., ACS Nano 10 (2016) 4496–4503.
[20] Z. Wang, Y. Liu, B. Huang, et al., Phys. Chem. Chem. Phys. 16 (2014) 2758–2774.
[21] D. Mateo, J.L. Cerrillo, S. Durini, et al., Chem. Soc. Rev. 50 (2021) 2173–2210.
[22] J.D. Xiao, H.L. Jiang, Acc. Chem. Res. 52 (2019) 356–366.
[23] S. Luo, X. Ren, H. Lin, et al., Chem. Sci. 12 (2021) 5701–5719.
[24] Q. Zeng, J. Bai, J. Li, et al., Nano Energy 41 (2017) 225–232.
[25] Q. Zeng, S. Chang, A. Beyhaqi, et al., J. Hazard. Mater. 394 (2020) 121425.
[26] Q. Zhang, Y. Xiao, L. Yang, et al., Chin. Chem. Lett. 34 (2023) 107628.
[27] H. Liu, L. Shi, Q. Zhang, et al., Chem. Commun. 57 (2021) 1279–1294.
[28] Y. Zhou, D.E. Doronkin, Z. Zhao, et al., ACS Catal. 8 (2018) 11398–11406.
[29] N.L. Reddy, V.N. Rao, M. Vijayakumar, et al., Int. J. Hydrog. Energy 44 (2019) 10453–10472.
[30] Q. Zhang, W. Xu, X. Wang, Sci. China Mater. 61 (2018) 905–914.
[31] Y. Tang, W. Zhou, Q. Shang, et al., Appl. Catal. B: Environ. 310 (2022) 121295.
[32] D. Zhang, H. Wu, C.R. Bowen, et al., Small 17 (2021) 2103960.
[33] S. Zhang, Z. Zhang, Y. Si, et al., ACS Nano 15 (2021) 15238–15248.
[34] J. Zhu, W. Shao, X. Li, et al., J. Am. Chem. Soc. 143 (2021) 18233–18241.
[35] S. Guo, X. Li, J. Li, et al., Nat. Commun. 12 (2021) 1343.
[36] B. Tan, M. Sun, B. Liu, et al., Nano Energy 107 (2023) 108138.
[37] J.T. Robinson, S.M. Tabakman, Y. Liang, et al., J. Am. Chem. Soc. 133 (2011) 6825–6831.
[38] B. Dai, J. Fang, Y. Yu, et al., Adv. Mater. 32 (2020) 1906361.
[39] A. Mishra, P. Bauerle, Angew. Chem. Int. Ed. 51 (2012) 2020–2067.
[40] N. Jiang, X. Zhuo, J. Wang, Chem. Rev. 118 (2018) 3054–3099.
[41] H. Ren, M. Tang, B. Guan, et al., Adv. Mater. 29 (2017) 1702590.
[42] P. Cheng, H. Wang, B. Muller, et al., ACS Appl. Mater. Interfaces 13 (2021) 1818–1826.
[43] H. Jick, D.P. Chamberlin, K.W. Hagberg, Epidemiology 21 (2010) 270–271.
[44] C. Song, Z. Wang, Z. Yin, et al., Chem. Catal. 2 (2022) 52–83.
[45] M. Gao, C.K. Peh, L. Zhu, et al., Adv. Energy Mater. 10 (2020) 2000925.
[46] P. Cheng, D. Wang, P. Schaaf, Adv. Sustain. Syst. 6 (2022) 2200115.
[47] X. Wu, J. Wang, Z. Wang, et al., Angew. Chem. Int. Ed. 60 (2021) 9416–9420.
[48] H. Yang, L.Q. He, Y.W. Hu, et al., Angew. Chem. Int. Ed. 54 (2015) 11462–11466.
[49] N. Lu, Z. Zhang, Y. Wang, et al., Appl. Catal. B 233 (2018) 19–25.
[50] J. Peng, X. Yu, Y. Meng, et al., J. Chem. Phys. 152 (2020) 134704.
[51] X. Yu, Y. Zheng, Y. Wang, et al., Chem. Mater. 34 (2022) 1110–1120.
[52] Y. Zheng, S. Chen, X. Yu, et al., Appl. Surf. Sci. 598 (2022) 153786.
[53] M. Lv, C. Luo, J. Li, et al., ACS Mater. Lett. 5 (2023) 744–752.
[54] Y. Zheng, T. Gao, S. Chen, et al., Compos. Commun. 36 (2022) 101390.
[55] M. Zhu, L. Zhang, S. Liu, et al., Chin. Chem. Lett. 31 (2020) 1961–1965.
[56] D. Wang, A. Chen, S. Lai, et al., Chin. Chem. Lett. 34 (2023) 107861.
[57] P. Chen, Y. Mu, Y. Chen, et al., Chemosphere 291 (2022) 132817.
[58] L. Tian, L. Zhang, L. Zheng, et al., Angew. Chem. Int. Ed. 61 (2022) e202214145.
[59] X. Cheng, L. Wang, L. Xie, et al., Chem. Eng. J. 439 (2022) 135757.
[60] M. Moniruzzaman, J. Kim, Appl. Surf. Sci. 552 (2021) 149372.
[61] F. Flory, L. Escoubas, G. Berginc, J. Nanophotonics 5 (2011) 052502.
[62] D. McKenzie, M. Large, J. Exp. Biol. 201 (1998) 1307–1313.
[63] K. Mizuno, J. Ishii, H. Kishida, et al., Proc. Natl. Acad. Sci. U. S. A. 106 (2009) 6044–6047.
[64] P. Zhang, J. Li, L. Lv, et al., ACS Nano 11 (2017) 5087–5093.
[65] Z. Liu, Z. Yang, X. Huang, et al., J. Mater. Chem. A 5 (2017) 20044–20052.
[66] X. Hu, W. Xu, L. Zhou, et al., Adv. Mater. 29 (2017) 1604031.
[67] F. Zhao, X. Zhou, Y. Shi, et al., Nat. Nanotechnol. 13 (2018) 489–495.
[68] Y. Li, J. Xue, Q. Shen, et al., Chem. Eng. J. 423 (2021) 130188.
[69] J.W. Xu, K. Yao, Z.K. Xu, Nanoscale 11 (2019) 8680–8691.
[70] H.K. Bisoyi, A.M. Urbas, Q. Li, Adv. Opt. Mater. 6 (2018) 1–44.
[71] L. Zhu, M. Gao, C.K.N. Peh, et al., Mater. Horiz. 5 (2018) 323–343.
[72] Y. Li, X. Tian, L. Chen, et al., Bioelectrochemistry 147 (2022) 108195.
[73] S.G. Porter, Ferroelectrics 33 (2011) 193–206.
[74] A. Katti, Phys. Lett. A 458 (2023) 128590.
[75] B.P. Mishra, L. Biswal, S. Das, et al., Langmuir 39 (2023) 957–971.
[76] K. Zhang, C. Liu, F. Huang, et al., Appl. Catal. B 68 (2006) 125–129.
[77] S. Wang, G. Xue, J. Liang, et al., Catal. Commun. 45 (2014) 39–43.
[78] C. Dong, Z. Qu, Y. Qin, et al., ACS Catal. 9 (2019) 6698–6710.
[79] Z. Wei, C. Hsu, H. Almakrami, et al., Electrochim. Acta 316 (2019) 173–180.
[80] Y. Wang, L. Zhu, Y. Feng, et al., Adv. Funct. Mater. 29 (2018) 18886–18893.
[81] X.Q. Wang, C.F. Tan, K.H. Chan, et al., Nat. Commun. 9 (2018) 3438.
[82] Z. Wang, R. Yu, C. Pan, et al., Nat. Commun. 6 (2015) 8401.
[83] J. Liu, P. Chakraborty, H. Zhang, et al., ACS Catal. 9 (2019) 2610–2617.
[84] H. You, S. Li, Y. Fan, et al., Nat. Commun. 13 (2022) 6144.
[85] Y. Liu, Y.H. Li, X. Li, et al., ACS Nano 14 (2020) 14181–14189.
[86] W. Yin, L. Bai, Y. Zhu, et al., ACS Appl. Mater. Interfaces 8 (2016) 23133–23142.
[87] Z. Zhou, X. Niu, Y. Zhang, et al., J. Mater. 7 (2019) 21835–21842.
[88] X.H. Jiang, L.S. Zhang, H.Y. Liu, et al., Angew. Chem. Int. Ed. 59 (2020) 23112–23116.
[89] M. Guo, Y. Liu, S. Dong, et al., ChemSusChem 11 (2018) 4150–4155.
[90] H. Li, C. Tsai, A.L. Koh, et al., Nat. Mater. 15 (2016) 48–53.
[91] X. Zhang, F. Zhou, S. Zhang, et al., Adv. Sci. 6 (2019) 1900090.
[92] T. Wu, S. Sun, J. Song, et al., Nat. Catal. 2 (2019) 763–772.
[93] S. Zhang, Y. Si, B. Li, et al., Small 17 (2021) 2004980.
[94] W. Wu, C. Niu, C. Wei, et al., Angew. Chem. Int. Ed. 58 (2019) 2029–2033.
[95] H. Zhang, L. Yu, T. Chen, et al., Adv. Funct. Mater. 28 (2018) 1807086.
[96] H. Zhang, S. Zuo, M. Qiu, et al., Sci. Adv. 6 (2020) eabb9823.
[97] W. Karim, C. Spreafico, A. Kleibert, et al., Nature 541 (2017) 68–71.
[98] W.C. Conner, J.L. Falconer, Chem. Rev. 95 (1995) 759–788.
[99] K. Maeda, K. Teramura, D. Lu, et al., Angew. Chem. Int. Ed. 45 (2006) 7806–7809.
[100] P.T.H.M. Verhallen, L.J.P. Oomen, A.J.J.M.v.d. Elsen, et al., Chem. Eng. Sci. 39 (1984) 1535–1541.
[101] H.P. Nguyen, M. Djavid, K. Cui, et al., Nanotechnology 23 (2012) 194012.
[102] M. Wang, W. Zhen, B. Tian, et al., Appl. Catal. B 236 (2018) 240–252.
[103] M. Wang, Z. Li, Y. Wu, et al., J. Catal. 353 (2017) 162–170.
[104] P. Zhou, I.A. Navid, Y. Ma, et al., Nature 613 (2023) 66–70.
[105] T. Van Gerven, G. Mul, J. Moulijn, et al., Chem. Eng. Process. 46 (2007) 781–789.
[106] C. Li, D. Zhu, S. Cheng, et al., Chin. Chem. Lett. 33 (2022) 1141–1153.
[107] J. Cihlar, V. Kasparek, M. Kralova, et al., Int. J. Hydrog. Energy 40 (2015) 2950–2962.
[108] E. Bu, Y. Chen, C. Wang, et al., Chem. Eng. J. 370 (2019) 646–657.
[109] Y. Liu, Z. Liu, L. Jia, et al., Appl. Surf. Sci. 606 (2022) 154897.
[110] Y. Wang, W. Huang, S. Guo, et al., Adv. Energy Mater. 11 (2021) 2102452.
[111] H. Han, K. Huang, Y. Yao, et al., Chem. Eng. J. 450 (2022) 138419.
[112] M.D. Scanlon, P. Peljo, L. Rivier, et al., Phys. Chem. Chem. Phys. 19 (2017) 22700–22710.
[113] G. Liu, X. Gao, K. Wang, et al., Int. J. Hydrog. Energy 41 (2016) 17976–17986.
[114] Y. Zhang, P. Guo, S. Guo, et al., Angew. Chem. Int. Ed. 61 (2022) 202209703.
[115] Y. Zhang, T. Gao, S. Chen, et al., Compos. Commun. 36 (2022) 101390.
[116] Y. Zhang, S. Chen, X. Yu, et al., Appl. Surf. Sci. 598 (2022) 153786.
[117] Y. Zhang, X. Ni, K. Li, et al., Compos. Commun. 32 (2022) 101116.